SWAN SurfBeat-1D

Reniers, Ad; Zijlema, Marcel

DOI
10.1016/j.coastaleng.2021.104068

Publication date
2022

Document Version
Final published version

Published in
Coastal Engineering

Citation (APA)
Reniers, A., & Zijlema, M. (2022). SWAN SurfBeat-1D. *Coastal Engineering*, *172*, Article 104068. https://doi.org/10.1016/j.coastaleng.2021.104068

Coastal Engineering 172 (2022) 104068

Contents lists available at ScienceDirect

Coastal Engineering

journal homepage: www.elsevier.com/locate/coastaleng

SWAN SurfBeat-1D

Ad Reniers *, Marcel Zijlema

Delft University of Technology, Faculty of Civil Engineering and GeoSciences, Department of Hydraulic Engineering, Stevinweg 1, 2628CN, Delft, The Netherlands

ARTICLE INFO

Keywords:
Bound and free infragravity waves
Spectral modeling
Field and laboratory validation

ABSTRACT

The Simulating WAves Nearshore (SWAN) model has been extended with an infragravity module to predict the Wave-Group-Forced (WGF) infragravity response to a frequency-directional sea-swell spectrum at a mildly sloping alongshore uniform beach. To that end the SWAN model has been extended with an WGF-infragravity source term denoted S_{sb} where the subscript denotes surfbeat. The corresponding WGF infragravity energy model has been verified with a set of benchmark tests using the infragravity amplitude model of Reniers et al. (2002). Next the implementation of the energy balance in SWAN has been validated with both prototype-scale laboratory experiments and field observations, showing a good comparison with observations not affected by the nodal structure of the (partially) standing infragravity waves. This suggests that the model is capable of providing improved infragravity boundary conditions in relatively shallow water compared to the typical assumption of equilibrium forcing conditions using for instance Hasselmann's equilibrium theory (Hasselmann, 1962). These infragravity boundary conditions can subsequently can be used by other more sophisticated models to compute runup, overtopping and dune erosion.

1. Introduction

The frequency-directional spectrum of the incident sea-swell waves controls the wave interference patterns forming wave groups with periods between approximately 25 s to 250 s. This results in a modulation of the radiation stress, forcing bound infragravity waves that propagate with the wave groups (Biesel, 1952; Longuet-Higgins and Stewart, 1962; Hasselmann, 1962). As the wave groups approach the beach the sea-swell waves become gradually steeper and ultimately break dissipating their energy in the surfzone. As a result the wave-group modulation reduces and the bound infragravity waves get released and (partially) reflect at the shoreline (Herbers et al., 1995; Van Dongeren et al., 2007; Thompson et al., 2006). On mildly sloping beaches this can result in a dominance of the infragravity wave energy at the waterline (Holman, 1981; Guza and Thornton, 1982; Ruessink, 1998a,b; De Bakker et al., 2014), controlling the run-up and potential overtopping at the beach (e.g. Stockdon et al. (2006), Ruggiero et al. (2004) and Guza and Feddersen (2012)) as well as dune erosion (Van Thiel de Vries et al., 2008; Roelvink et al., 2007) and overwash [e.g. McCall et al. (2010)]. For a comprehensive review on infragravity waves refer to Bertin et al. (2018).

Modeling the impact of incident infragravity waves requires an offshore boundary condition. This boundary condition is usually obtained by assuming a local equilibrium between the incident sea-swell wave forcing and the bound infragravity wave (Hasselmann, 1962; Longuet-Higgins and Stewart, 1962). There are two potential problems with this approach. First, both phase-resolving modeling and observations have shown that the local equilibrium approach at times may significantly overestimate the sea-swell forced infragravity waves (Schäffer, 1993; Herbers and Burton, 1997; Battjes et al., 2004). This is related to the fact that the transfer of energy from the sea-swell waves to the underlying infragravity waves on a sloping bed needs time and thus distance to occur. In case the changes in water depth and accompanying sea-swell conditions are relatively fast with respect to the infragravity wave length the equilibrium condition is not reached. Secondly, by using the local equilibrium it is implicitly assumed that offshore only bound infragravity waves are incident on the coast. Ardhuin et al. (2014) and Rawat et al. (2014) have shown that infragravity waves generated at one coast can radiate away and propagate across oceanic scales where they arrive as free infragravity waves at another coast. This implies that the local equilibrium approximation may in fact underestimate the incident infragravity energy. This contribution of the free infragravity waves to the total infragravity spectrum will depend, among other things, on the coastal configuration, where a larger part of the infragravity energy can be trapped on the sloping bathymetry with increasing offshore water depth (Herbers et al., 1995; Smit et al., 2018). As a result the free infragravity energy arriving from distant storms is relatively unimportant along open coasts when the local sea-swell forcing is significant (Smit et al., 2018). However, in regional seas where the offshore water depth is limited, a significant part of the

* Corresponding author.
E-mail address: a.j.h.m.reniers@tudelft.nl (A. Reniers).

https://doi.org/10.1016/j.coastaleng.2021.104068
Received 15 September 2020; Received in revised form 4 October 2021; Accepted 27 November 2021
Available online 17 December 2021

infragravity energy may travel from coast to coast affecting the local infragravity conditions (Rijnsdorp et al., 2021) and subsequent runup and associated coastal safety during severe storms. Hence, depending on the coastal configuration, the local equilibrium approximation may result in an overestimation or underestimation of the incident infragravity waves. Refer to Fiedler et al. (2019) for an assessment of the infragravity wave boundary effects on runup and wave shape. These boundary problems can be overcome by using a much larger regional-scale infragravity model domain with the offshore boundary condition located in deeper water.

However, computing infragravity waves at a regional scales (O(100) km) prevents the use of deterministic models as they need a fine numerical grid to resolve the infragravity waves leading to very long computational times. This can be overcome by considering the wave energy balance of the infragravity waves using spatial propagation, source and sink terms to describe the evolution over long time and spatial scales. This approach is used to describe the evolution of sea-swell waves at global scales with WaveWatch 3 (Tolman, 1991) and WAM (Hasselmann et al., 1988) as well as regional scales using SWAN (Booij et al., 1999) and Tomawac (Benoit et al., 1996). To be able to compute the infragravity energy balance, the non-linear source term describing the transfer of energy from the incident waves to the infragravity waves needs to be included. This requires an evolution equation of the triad interaction between two incident waves making up a wave group and the accompanying forced infragravity wave (Phillips, 1977; Madsen and Sorensen, 1993; Herbers and Burton, 1997). Eldeberky and Battjes (1995) formulated a source term in SWAN, S_{nl3}, to describe the generation and evolution of forced super harmonics within the spectrum. To be able to describe the evolution of the infragravity energy balance this term needs to be complemented with a source term for the forced subharmonics that we will denote S_{sb} where the subscript sb stands for surfbeat.[1]

To expedite computations SWAN uses a Lumped Triad Approximation (LTA) (Eldeberky and Battjes, 1995), considering self interactions of co-linear waves only to represent S_{nl3}. The LTA makes use of a non-linear coupling function based on the work by Madsen and Sorensen (1993) and an estimate of the bi-phase with a parametrization based on the local Ursell number to compute S_{nl3}. The expression for the bi-phase predicts the phase coupling between the two primary waves and the forced super harmonic thus controlling the skewness and asymmetry of the incident waves (Elgar and Guza, 1985). This superharmonic bi-phase is different from the phase coupling of the sea-swell waves with the forced sub-harmonics and the local Ursell parametrization of Eldeberky and Battjes (1995) can therefore not be used. Furthermore, the LTA considers self interactions only, whereas the infragravity waves are forced by difference interactions, requiring a different description for the non-linear coupling. And finally, the LTA uses co-linear waves only, whereas the forced infragravity waves typically have a much broader directional distribution resulting from the directional spreading of the sea-swell waves forcing them (Herbers and Burton, 1997). Instead, as a first step, the non-linear subharmonic coupling and accompanying bi-phase in the presence of directional sea-swell waves at an alongshore uniform coast are derived making use of the radiation stress concept (Longuet-Higgins and Stewart, 1964) following Reniers et al. (2002), Janssen et al. (2003) and Battjes et al. (2004). This results in a directional infragravity energy source term, S_{sb}, that is used to predict the evolution of the wave-group-forced infragravity wave energy described in Section 2. Predictions with this infragravity energy model are first compared with the infragravity amplitude model developed by Reniers et al. (2002) for simplified conditions in Section 3.1. Next the infragravity energy balance is implemented in SWAN and compared with both large scale laboratory experiments in Section 3.2 and field observations in Section 3.3. The general applicability and model limitations are discussed in Section 4 in view of potential applications at the regional scale followed by conclusions in Section 5.

[1] The infragravity waves associated with breaking wave groups was coined surfbeat by Munk (1949).

2. Methods

2.1. Infragravity Amplitude Model (IAM)

The wave-group-forced (WGF in the following) infragravity model developed by Reniers et al. (2002) is based on the linearized shallow water equations (Mei and Benmoussa, 1984). This model has been compared with both analytical solutions and field observations showing a good correspondence (Reniers et al., 2002, 2010) making it a suitable benchmark. A brief description of the model is presented here for ease of reference. The spectral WGF long wave equation is given by:

$$gh\frac{d^2\hat{\eta}}{dx^2} + g\frac{dh}{dx}\frac{d\hat{\eta}}{dx} + \Delta\omega^2\hat{\eta} - gh\Delta k_y^2\hat{\eta} = -\frac{1}{\rho}\left(\frac{d^2\hat{S}_{xx}\exp i\int_0^x \Delta k_x dx}{dx^2} + 2i\Delta k_y\frac{d\hat{S}_{xy}\exp i\int_0^x \Delta k_x dx}{dx} - \Delta k_y^2\hat{S}_{yy}\exp i\int_0^x \Delta k_x dx\right) \quad (1)$$

where x and y are directed onshore and alongshore respectively, h is the local water depth, g the gravitational acceleration, $\hat{\eta}$ is the complex valued infragravity surface elevation amplitude.

Considering the short-wave group to be made up of two incident sea-swell components with amplitudes a_1 and a_2, frequencies ω_1 and ω_2 and directions θ_1 and θ_2 respectively, the corresponding radiation stress amplitudes at the right hand side are given by:

$$\hat{S}_{xx} = \left(\frac{c_g}{c}(1+\cos^2\alpha) - \frac{1}{2}\right)\rho g a_1 a_2 \quad (2)$$

and

$$\hat{S}_{xy} = \frac{c_g}{c}(\cos\alpha\sin\alpha)\rho g a_1 a_2 \quad (3)$$

and

$$\hat{S}_{yy} = \left(\frac{c_g}{c}(1+\sin^2\alpha) - \frac{1}{2}\right)\rho g a_1 a_2 \quad (4)$$

representing the slow modulation of the radiation stresses related to mild changes in depth. The corresponding phase velocity, c and group velocity, c_g, are computed with linear wave theory using the mean frequency of the two components. The bi-chromatic wave group creates a modulation in the radiation stress with difference frequency $\Delta\omega = \omega_2 - \omega_1$, difference cross-shore wave number $\Delta k_x = k_{2,x} - k_{1,x}$ and alongshore wave number $\Delta k_y = k_{2,y} - k_{1,y}$ forcing an infragravity response. In case of an alongshore uniform beach the alongshore wave number is constant, whereas the cross-shore wave number changes with depth, hence the integral in the phase function to represent the modulation at the wave group scale in the cross-shore direction in Eq. (1) . Given the fact that the wave direction of the individual sea-swell waves, θ_1 and θ_2, can be computed with Snel's law in case of an alongshore uniform beach, the difference wave numbers are readily retrieved and the mean sea-swell wave direction α is subsequently obtained from:

$$\alpha = atan\left(\frac{k_{1,y} + k_{2,y}}{k_{1,x} + k_{2,x}}\right) \quad (5)$$

Given the offshore boundary conditions for the two incident waves and a bottom profile the slow cross-shore variation in the radiation stress forcing, $S_{ij}(x)$, can be computed with a mean wave energy balance taking into account shoaling, refraction and wave breaking. Next, with the appropriate boundary conditions, the complex infragravity wave amplitudes can be computed with Eq. (1). The corresponding infragravity surface elevation can be re-constructed from the complex amplitudes through:

$$\eta(x,y,t) = \Re\left(\hat{\eta}(x)\exp(i(\Delta\omega t - \Delta k_y y))\right) \quad (6)$$

where $\Re$ corresponds to the real part and similar expressions are used for the wave-group modulation and infragravity velocities (see

Reniers et al., 2002 for details). The fully reflective shoreline boundary condition of Reniers et al. (2002) has been replaced with an absorbing boundary condition to retain the incident infragravity waves only to facilitate the comparison with the WGF infragravity energy balance discussed next.

2.2. Infragravity Energy Model (IEM)

Instead of solving for the infragravity surface elevation amplitude with Eq. (1), an infragravity energy balance can be used in combination with a non-linear source term to account for the transfer of energy from the sea-swell wave group to the accompanying WGF infragravity wave. To that end we extend the normally incident approach of Battjes et al. (2004) by defining the steady state wave energy balance for obliquely incident WGF infragravity waves on a mildly sloping, alongshore uniform beach (Phillips, 1977):

$$\frac{\partial F_x}{\partial x} = S_{sb} \tag{7}$$

where F_x is the cross-shore infragravity energy flux and S_{sb} represents the source term associated with the forcing by a bichromatic wave train made up of two obliquely incident sea-swell components. The energy flux F_x in Eq. (7), is approximated using the velocity potential for the long waves (Battjes et al., 2004):

$$F_x = -\rho h \overline{\frac{\partial \phi}{\partial t}\frac{\partial \phi}{\partial x}} \tag{8}$$

where the overline corresponds to wave-group averaging. The time derivative of the velocity potential corresponds to the combined instantaneous kinetic and potential energy of the infragravity wave motion that is subsequently transported by the cross-shore component of the instantaneous velocity of the WGF long wave:

$$\frac{\partial \phi}{\partial x} = U_{f,x} = U_f \cos\theta_f \tag{9}$$

where the subscript f stands for the WGF motion. The direction of the WGF infragravity wave is obtained from the refraction of the two individual sea-swell waves making up the wave group:

$$\theta_f = atan\left(\frac{\Delta k_y}{\Delta k_x}\right) \tag{10}$$

and the corresponding alongshore infragravity velocity is given by $U_{f,y} = U_f \sin\theta_f$. For a mildly sloping cross-shore profile the time derivative in Eq. (8) can be approximated as:

$$\frac{\partial}{\partial t} = \frac{-c_g}{\cos\theta_f}\frac{\partial}{\partial x} \tag{11}$$

which upon substitution in Eq. (8) yields the WGF-infragravity energy flux equation:

$$F_x = \frac{\rho c_g h}{\cos\theta_f}\overline{\left(\frac{\partial \phi}{\partial x}\right)^2} = \frac{\rho c_g h}{\cos\theta_f}\overline{U_{f,x}^2} = \frac{\rho}{2} c_g h \hat{U}_f^2 \cos\theta_f \tag{12}$$

where $\hat{U}_f$ corresponds to the velocity amplitude of the WGF-infragravity wave.

To solve the infragravity energy balance the right-hand side of Eq. (7) has to be evaluated next. The source term S_{sb} corresponds to the work done by the radiation stresses on the WGF-infragravity wave in the presence of obliquely incident waves (Phillips, 1977):

$$S_{sb} = -\overline{U_{f,x}\frac{\partial S_{xx}}{\partial x}} - \overline{U_{f,y}\frac{\partial S_{xy}}{\partial y}} \tag{13}$$

operating in both the cross-shore and alongshore direction in the presence of obliquely incident waves. In case the forcing is a wave group made up by two sea-swell components with different frequencies and directions, S_{sb} can be approximated by (following the approach by Battjes et al. (2004)):

$$S_{sb} = \frac{1}{2}\Delta k_x \hat{U}_{f,x}\hat{S}_{xx}\sin\Delta\psi + \frac{1}{2}\Delta k_y \hat{U}_{f,y}\hat{S}_{xy}\sin\Delta\psi + \frac{1}{2}\hat{U}_{f,x}\frac{\partial \hat{S}_{xx}}{\partial x}\cos\Delta\psi \tag{14}$$

with the radiation stress amplitudes, $\hat{S}_{ij}$, given by Eqs. (2)–(4) and the bi-phase, $\Delta\psi$, represents the phase coupling between the radiation stress forcing and the accompanying WGF infragravity wave. The first two terms on the right hand side are related to the harmonic modulation of the wave group and the third term is related to the slow changes in the radiation stress amplitude due to cross-shore depth variations. Combining the left hand side and right hand side the WGF-infragravity energy balance, Eq. (7) can be written as:

$$\frac{\rho}{2}\frac{\partial c_g \cos\theta_f h \hat{U}_f^2}{\partial x} = \frac{1}{2}\left(\Delta k_x \hat{U}_{f,x}\hat{S}_{xx} + \Delta k_y \hat{U}_{f,y}\hat{S}_{xy}\right)\sin\Delta\psi + \frac{\hat{U}_{f,x}}{2}\frac{\partial \hat{S}_{xx}}{\partial x}\cos\Delta\psi \tag{15}$$

To compute the non-linear transfer the bi-phase, $\Delta\psi$, needs to be known as well. To that end the WKB-based expression derived by Janssen et al. (2003) is extended to provide the evolution equation for the bi-phase for obliquely incident waves resulting in (see Appendix A):

$$\begin{aligned}\frac{d\Delta\psi}{dx} = &-\frac{\Delta k_x \mu}{2} + \frac{\hat{S}_{xx}}{2\,gh|\hat{\eta}_f|}\\ &\times\left(\Delta k_x\cos\Delta\psi - \left(\frac{2}{\hat{S}_{xx}}\frac{d\hat{S}_{xx}}{dx} - \frac{\cos\theta_f}{c_g}\frac{dc_g(\cos\theta_f)^{-1}}{dx}\right)\sin\Delta\psi\right)\\ &+\frac{\hat{S}_{xy}}{gh|\hat{\eta}_f|}\left(\Delta k_y\cos\Delta\psi - \frac{\Delta k_y}{\Delta k_x}\left(\frac{1}{\hat{S}_{xy}}\frac{\partial \hat{S}_{xy}}{\partial x}\right)\sin\Delta\psi\right)\\ &-\frac{\hat{S}_{yy}}{2\,gh|\hat{\eta}_f|}\left(\frac{\Delta k_y^2}{\Delta k_x}\right)\sin\Delta\psi\end{aligned} \tag{16}$$

where μ represents the resonant mismatch:

$$\mu = \left(1 - \frac{\Delta\omega^2 - gh\Delta k_y^2}{gh\Delta k_x^2}\right) \tag{17}$$

Summarizing, the infragravity energy model consists of two coupled equations, Eq. (15) for the infragravity energy and Eq. (16) for the bi-phase, that need to be solved in tandem. Note that the evolution equation of the bi-phase depends on the WGF infragravity surface elevation, $\hat{\eta}_b$, that can be expressed as function of the WGF infragravity velocity $\hat{U}_f$ using the continuity equation assuming a mild bed-slope:

$$\hat{U}_f = \hat{\eta}_f \frac{c_g}{h} \tag{18}$$

leaving two unknowns, i.e. $\hat{U}_f$ and $\Delta\psi$, that can be solved for a given offshore boundary condition. For F_x this is given by the incoming energy flux of the WGF infragravity wave at $x = 0$:

$$F_{x,0} = \frac{1}{2}\rho c_{g,0} cos\theta_{f,0} h_0 \hat{U}_{f,0}^2 \tag{19}$$

where the subscript 0 refers to the conditions at $x = 0$ m. Using Eq. (18) the offshore WGF velocity is given by:

$$\hat{U}_{f,0} = \hat{\eta}_{f,0}\frac{c_{g,0}}{h_0} = \frac{\hat{S}_{xx,0} + 2\hat{S}_{xy,0}\frac{\Delta k_y}{\Delta k_{x,0}}}{\mu_0\, gh_0}\frac{c_{g,0}}{h_0} \tag{20}$$

where the corresponding WGF surface elevation, $\hat{\eta}_{f,0}$, is based on a horizontal bed with a bi-phase of 0° corresponding to the offshore boundary condition of $\Delta\psi$ (see Appendix A). Casting the coupled differential equations in finite difference form using an upwind scheme the WGF infragravity energy, amplitude and bi-phase can be integrated along the x-axis (see Appendix B) and subsequently be compared with the IAM results.

2.3. SWAN implementation

2.3.1. Sea-swell forced infragravity energy

SWAN (Booij et al., 1999) computes the evolution of the frequency-directional sea-swell spectrum, $E(\omega,\theta)$ with the angular frequency ω

larger than the infragravity frequency cut-off ω_c, subject to refraction, shoaling and sink and source terms, $S(\omega,\theta)$, related to bottom friction, wave breaking, white capping, non-linear interactions and wind forcing. Assuming stationary conditions subject to wave breaking only the wave energy balance reduces to:

$$\frac{\partial E(\omega,\theta)c_{g,x}}{\partial x}+\frac{\partial E(\omega,\theta)c_{g,y}}{\partial y}+\frac{\partial E(\omega,\theta)c_{\theta}}{\partial \theta}=-S_{br}(\omega,\theta) \tag{21}$$

where $c_{g,x}$, $c_{g,y}$ and c_θ are the energy density transport velocities in x, y and θ direction respectively. Wave breaking, S_{br}, is computed with the dissipation model of Battjes and Janssen (1978) with γ_b as a calibration coefficient controlling the maximum sea-swell wave height, $H_{max}=\gamma_b h$. Given a bathymetry and an offshore sea-swell boundary condition the frequency-directional spectrum can be solved for (Booij et al., 1999).

To include infragravity waves in SWAN with frequencies less or equal to ω_c Eq. (15) is used, which is representative for the forcing by a single bichromatic group. However, in the presence of a realistic directionally spread sea-swell wave field all frequency-directional pairs with a difference frequency less or equal to the infragravity frequency cutoff, ω_c, create bichromatic wave groups contributing to the WGF source term S_{sb}. For a specific combination within the frequency-directional spectrum this contribution to the radiation stresses can be expressed as:

$$\hat{S}_{xx}(\Delta\omega,\Delta k_y)=\rho g\left(\frac{c_g}{c}(1+\cos^2\alpha)-\frac{1}{2}\right)a_{p,n}a_{q,m} \tag{22}$$

and

$$\hat{S}_{xy}(\Delta\omega,\Delta k_y)=\rho g\frac{c_g}{c}(\cos\alpha\sin\alpha)a_{p,n}a_{q,m} \tag{23}$$

where the difference frequency is given by $\Delta\omega=\omega_q-\omega_p$ and the difference alongshore wave number is given by $\Delta k_y=k_q sin(\theta_m)-k_p sin(\theta_n)$, with p and q referring to the frequency bins and n and m to the directional bins in the offshore frequency-directional sea-swell spectrum. The corresponding amplitudes are obtained from:

$$a_{i,j}=\sqrt{2E(\omega_i,\theta_j)\delta\omega\delta\theta} \tag{24}$$

with i and j representing the frequency and directional bins and $\delta\theta$ and $\delta\omega$ corresponding to the directional and frequency resolution of the sea-swell spectrum computed with Eq. (21). Instead of tracing the slow amplitude evolution of the individual frequency-directional wave components, $a_{p,n}$ and $a_{q,m}$, the cross-shore distribution of the radiation stress amplitudes is obtained by scaling the offshore modulation of each pair with changes in the total variance according to:

$$a_{p,m}a_{q,m}(x)=a_{p,m}a_{q,m}|_{x=0}\frac{\frac{1}{2}\Sigma_i\Sigma_j a^2_{i,j}(x)}{\Sigma_i\Sigma_j\frac{1}{2}a^2_{i,j}|_{x=0}}\left(1-Q_b(x)\right) \tag{25}$$

Furthermore, to account for the fact that the modulation is partly reduced in the breakerzone, e.g. Schäffer and Svendsen (1988) and De Bakker et al. (2015), the modulation is reduced proportional to the fraction of breaking waves, Q_b, obtained with (Baldock et al., 1998):

$$Q_b=\exp\left(-\left(\frac{H_{max}}{H_{m0}}\right)^2\right) \tag{26}$$

with H_{m0} as the significant sea-swell wave height.

Within SWAN the phase and group velocity in Eqs. (15), (22) and (23), have been computed with the mean wave period, T_{m-10}, using linear wave theory where:

$$T_{m-10}=\frac{2\pi\int_{\omega_c}^{\omega_{max}}\int_0^{2\pi}\omega^{-1}E(\omega,\theta)d\theta d\omega}{\int_{\omega_c}^{\omega_{max}}\int_0^{2\pi}E(\omega,\theta)d\theta d\omega} \tag{27}$$

with ω_c as the infragravity frequency cutoff and ω_{max} as the maximum sea-swell frequency. For a specific pair of incident waves Eq. (15) yields the cross-shore distribution of the WGF velocity, $\hat{U}_f(\Delta\omega,\theta_f)$ and surface elevation $\hat{\eta}_f(\Delta\omega,\theta_f)$. The corresponding WGF surface elevation variance is given by:

$$S_f(\Delta\omega,\theta_f)=\frac{1}{2}\hat{\eta}^2_f(\Delta\omega,\theta_f) \tag{28}$$

Solving Eq. (15) for all possible $((p,m),(q,n))$ pairs with $\Delta\omega\le\omega_c$ and collecting terms with the same difference frequency and directional bin yields the total WGF forced surface elevation spectrum:

$$E_f(\Delta\omega,\theta)=\frac{\Sigma S_f(\Delta\omega,\theta_f)}{\delta\Delta\omega\delta\theta} \tag{29}$$

The corresponding incident sea-swell root-mean-square (RMS) wave height is defined as:

$$H_{rms,hi,c}=2\sqrt{2}\sqrt{\int_{\omega_c}^{\omega_{max}}\int_{-\pi/2}^{\pi/2}E(\omega,\theta)d\theta d\omega} \tag{30}$$

where θ is defined with respect to the shore normal. The concurrent WGF RMS wave height is given by:

$$H_{rms,lo,f}=2\sqrt{2}\sqrt{\int_{\omega_{min}}^{\omega_c}\int_{-\pi/2}^{\pi/2}E_f(\Delta\omega,\theta)d\theta d\Delta\omega} \tag{31}$$

with ω_{min} as the minimum angular infragravity frequency.

2.3.2. Reflected infragravity energy

The sea-swell forced infragravity waves are assumed to reflect at the shoreline. This is achieved by defining an outgoing infragravity energy flux at a minimal depth, h_c:

$$F_{r,h_c}=\frac{1}{2}\rho h_c\sqrt{gh_c}r_c^2\hat{U}^2_{f,h_c}cos(\theta_r) \tag{32}$$

where r_c is a reflection coefficient. The outgoing angle of the reflected infragravity wave is computed according to:

$$\theta_r=\pi-\theta_f \tag{33}$$

assuming specular reflection at a shoreline aligned with the y-direction. Given the fact that the outgoing infragravity waves are free they can be modeled with the regular wave energy balance equation, Eq. (21), applied to the reflected infragravity waves:

$$\frac{\partial E_r(\Delta\omega,\theta)c_{g,x}}{\partial x}+\frac{\partial E_r(\Delta\omega,\theta)c_{\theta}}{\partial\theta}=0 \tag{34}$$

thus simulating inverse shoaling and refraction. Depth-limited wave breaking is assumed not to affect the dissipation of reflected infragravity waves and hence absent in the infragravity energy balance Eq. (34). The reflected infragravity rms wave height is given by:

$$H_{rms,lo,r}=2\sqrt{2}\sqrt{\int_{\omega_{min}}^{\omega_c}\int_{-\pi}^{\pi}E_r(\Delta\omega,\theta)d\theta d\Delta\omega} \tag{35}$$

which is integrated over the full directional width to account for potential refractive trapping. The predicted total RMS infragravity wave height is given by the square root of the combined variances:

$$H_{rms,lo,c}=\sqrt{H^2_{rms,lo,f}+H^2_{rms,lo,r}} \tag{36}$$

thus ignoring phase locking between the incoming and outgoing infragravity waves associated with standing wave patterns.

2.4. Laboratory observations

The laboratory observations were obtained during the LIP11D prototype scale morphodynamic experiments in the Delta Flume (Arcilla et al., 1994; Roelvink and Reniers, 1994). These experiments considered a range in wave conditions corresponding to random unidirectional sea and swell waves represented by a Jonswap spectrum (see Table 1).

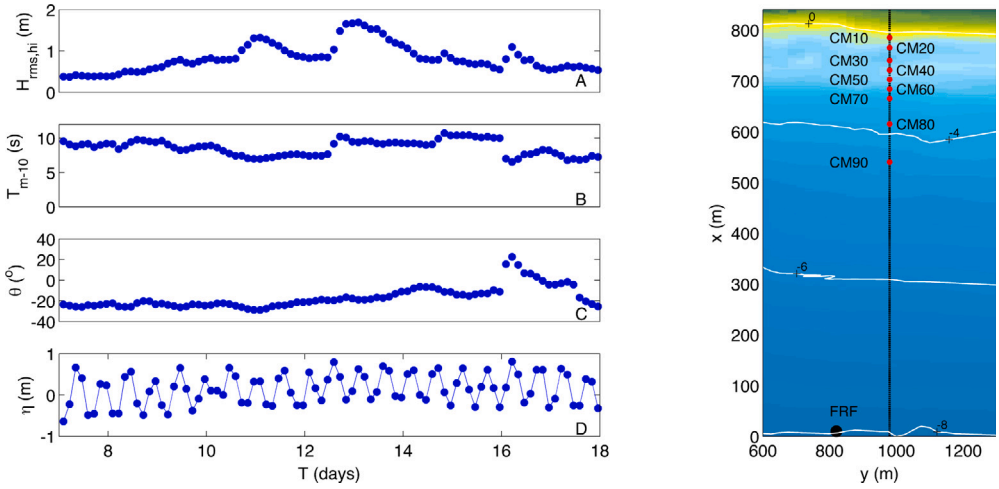

Fig. 1. Three-hourly FRF-8 m array conditions in October 1990. Panel A: Root mean square sea-swell wave height. Panel B: $T_{m,-10}$ wave period. Panel C: Mean wave direction with respect to the shore normal. Panel D: Tidal elevation. Right panel: FRF (black dot) and array (red dots) instrument locations. Depth contour lines (white) in meters below mean sea level. (For interpretation of the references to color in this figure legend, the reader is referred to the web version of this article.)

Table 1
Overview of LIP11D test wave conditions with $H_{m0,hi}$ and T_p as the significant sea-swell wave height and the peak period respectively.

Test case	1C0102	2A0102	2B0506
$H_{m0,hi}$ (m)	0.6	1.0	1.4
T_p (s)	8	5	5

The wave paddle was operated for an hour for a specific wave condition after which the bed elevation changes were measured to monitor the profile evolution. The hourly wave transformation was measured with ten fixed pressure sensors operating at 10 Hz. Using linear wave theory the pressure spectrum was translated to the surface elevation, $E_{\eta\eta}$, to obtain the sea-swell and infragravity wave heights given by:

$$H_{rms,hi,m} = 2\sqrt{2}\sqrt{\int_{0.05\ \mathrm{Hz}}^{0.3\ \mathrm{Hz}} E_{\eta\eta}(f)df} \tag{37}$$

with the subscript hi referring to the sea-swell band and m denotes measurements. The corresponding root mean square low frequency or infragravity wave height is given by:

$$H_{rms,lo,m} = 2\sqrt{2}\sqrt{\int_{0.01\ \mathrm{Hz}}^{0.04\ \mathrm{Hz}} E_{\eta\eta}(f)df} \tag{38}$$

At five locations colocated measurements of velocity have been used to separate the incoming and outgoing infragravity wave heights using the method of Guza et al. (1984), allowing a direct comparison with the model predictions of the incoming and reflected infragravity wave heights given by Eqs. (31) and (35) respectively. This method uses the shallow water phase speed for both incoming and reflected IG waves, whereas bound IG waves propagate with the group velocity. As the deepest sensor is located in approximately 2 m water depth the differences between the group velocity and the shallow water wave speed at all sensor locations is less than 15% for the conditions considered here. This results in minor differences in the estimated incoming and reflected IG wave heights if the group velocity is used for the incoming IG waves.

2.5. Field observations

The field data were collected during an eleven day period in October of 1990 at Duck, North Carolina as part of the DELILAH field experiment. Offshore sea-swell frequency-directional spectra were obtained from the Field Research Field (FRF) pressure array at 8 m water depth (right panel of Fig. 1) at a three-hourly interval. During this time the incident wave conditions ranged from mild to moderate with a maximum root mean square wave height of 1.75 m (Panel A in Fig. 1). Local wave conditions were predominantly due to a North-Easterly swell resulting in long period waves (panel B in Fig. 1) with an oblique incidence angle of approximately 25° with the shore normal. The tidal range was in the order of 1 m and predominantly vertical (panel D in Fig. 1). The wave transformation was measured with a cross-shore array of pressure sensors starting at an approximate water depth of 4 m (right panel of Fig. 1).

Linear wave theory is used to translate the corresponding pressure spectra to surface elevation spectra from which the root mean square sea-swell and infragravity wave heights have been computed according to Eqs. (37) and (38) using the same frequency intervals. In addition a bi-spectral analysis (Hasselmann et al., 1963; Herbers et al., 1994), is used to compute the bound root mean square infragravity wave height:

$$H_{rms,b,m} = 2\sqrt{2}\sqrt{\int_{0.01\ \mathrm{Hz}}^{0.04\ \mathrm{Hz}} E_{\eta_b\eta_b}(f)df} \tag{39}$$

where the bound variance density at the infragravity frequency Δf is given by:

$$E_{\eta_b\eta_b}(\Delta f) = \frac{2\int_{\Delta f}^{0.3-\Delta f} B(f,\Delta f)df}{\left[2\int_{\Delta f}^{0.3-\Delta f} E(f+\Delta f)E(f)E(\Delta f)df\right]^{\frac{1}{2}}} \tag{40}$$

with B as the bispectrum and a high-frequency cutoff of 0.3 Hz to avoid excessive amplification due to depth attenuation at higher frequencies.

2.6. Error metrics

To evaluate the model performance three error metrics are considered. The root mean square error is given by:

$$\epsilon(H) = \sqrt{\overline{(H_p - H_o)^2}} \tag{41}$$

where the subscript p refers to the predictions and o to the observations of variable H. The overbar indicates averaging over all relevant observations. The bias between predictions and observations is given by:

$$b(H) = \overline{H_p - H_o} \tag{42}$$

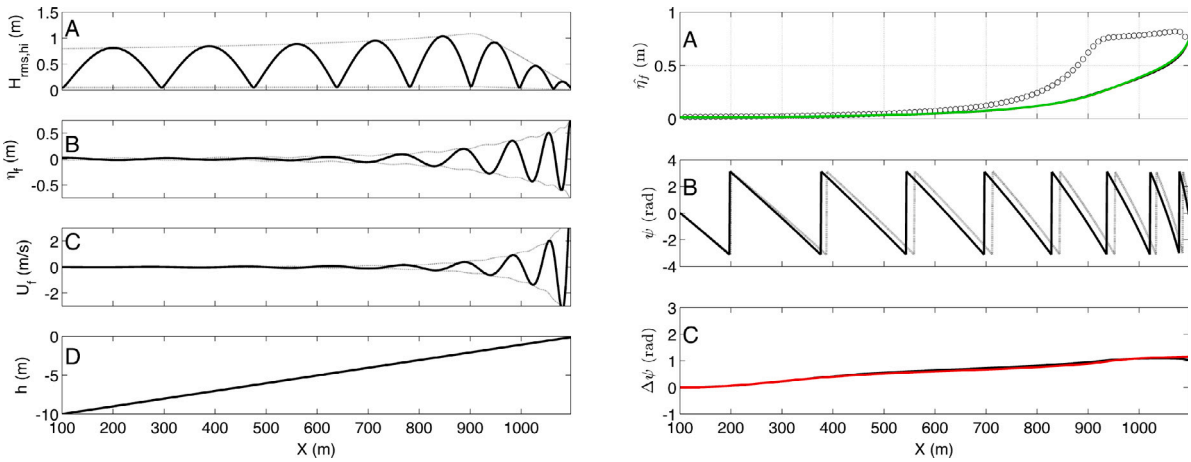

Fig. 2. Left Panels: IAM predictions for a normally incident bi-chromatic wave train with frequency difference of 0.04 Hz. Panel A: Snapshot of wave-group varying wave height (solid line) and corresponding envelope (dashed line). Panel B: Snapshot of concurrent WGF infragravity surface elevation (solid line) and corresponding envelope (dashed lines). Panel C: Similar for the cross-shore infragravity velocity. Panel D: Corresponding bed elevation. Right panels: Panel A: IAM-predicted (thick black line) and IEM-predicted (thick red line) WGF infragravity wave amplitude. Equilibrium solution of Longuet-Higgins and Stewart (1964) is given by the open circles as a reference. Panel B: IAM-predicted phase of the wave group forcing (dashed) and the accompanying WGF infragravity wave (solid). Panel C: IAM-predicted bi-phase (black) compared with IEM-prediction (red).

The corresponding scatter index is given by:

$$sci(H) = 1 - \frac{\epsilon(H)}{max(\sigma(H_o), \bar{H}_o)} \tag{43}$$

with σ as the standard deviation.

3. Verification and validation

For the verification of the Infragravity Energy Model (IEM) the infragravity response to a simple wave-group forcing made up of two incident sea-swell components of different frequencies and directions is compared with the IAM benchmark results. Model validation is performed in two steps. First by comparing the predicted, unidirectional infragravity response to normally incident random waves with large scale laboratory observations obtained during the LIP11D experiments in the Delta Flume as described in Section 2.4. Secondly by comparing the predicted directional infragravity response to frequency-directional sea-swell forcing observed during the Delilah field experiment at Duck, North Carolina as described in Section 2.5.

3.1. Benchmark testing

To compare the IEM with the IAM predictions of the WGF infragravity waves the setup of the numerical experiments performed by Herbers and Burton (1997) is used. These experiments reflect typical conditions at Duck, NC, with a constant slope of 0.01 starting at a water depth op 10 m (panel D on the left in Fig. 2). Herbers and Burton (1997) considered intermediate depths only, ranging from 10 m offshore to 4 m onshore. Here the model domain is extended to the water line with a minimal depth of 0.1 m with a constant grid spacing of 1 m. The wave group forcing is made up of two sea-swell components with a range of different frequencies and directions. The first subset consists of normally incident wave groups with a frequency difference ranging between 0.01 and 0.05 Hz centered around a mean frequency of 0.1 Hz. The second subset is made up of obliquely incident wave groups with a fixed frequency difference of 0.04 Hz centered around a mean frequency of 0.1 Hz. In these latter experiments the longer sea-swell component is kept at normal incidence whereas the shorter one varies between normally incident and 60° in deep water. The conditions for both subsets are summarized in Table 2.

Starting with a normally incident wave group made up of two sea-swell waves with frequencies of 0.08 Hz and 0.12 Hz respectively and corresponding deep water amplitudes of 0.2 m (see Table 2). The wave

Table 2
Deep water conditions for the numerical experiments of Herbers and Burton (1997). The frequency increment in subset 1 is 0.005 Hz whereas the directional increment in subset 2 is 5°. Deep water wave amplitudes are set at 0.2 m for all components.

Subset	f_1 (Hz)	f_2 (Hz)	θ_1(°)	θ_2(°)
1	From 0.095 to 0.075	From 0.105 to 0.1250	0	0
2	0.08	0.12	0	From 0 to 60

height modulation varies between 0 and 0.8 m offshore (left panel A of Fig. 2). Wave breaking starts around $x = 900$ m after which the modulation amplitude quickly decreases. Both the IAM-predicted WGF infragravity surface elevation and velocity increase non-linearly with decreasing depth (left panels B and C in Fig. 2). The IAM-predicted WGF infragravity amplitude is generally lower than the equilibrium solution of Longuet-Higgins and Stewart (1964) (right panel A in Fig. 2). This is consistent with the results of Schäffer (1993), the observations of Battjes et al. (2004) and the experiments by Herbers and Burton (1997). Computing the difference in phase between the forced infragravity wave and the corresponding wave group forcing (right panel B of Fig. 2) yields the bi-phase at every location (right panel C in Fig. 2). Next we solve for the coupled wave energy flux and bi-phase with the IEM showing a favorable comparison with both the IAM-computed WGF infragravity wave amplitude (right panel A of Fig. 2) and the corresponding bi-phase (right panel C of Fig. 2).

The next example considers a bi-chromatic wave made up of the same two sea-swell frequencies of 0.08 Hz and 0.12 Hz where the latter is now obliquely incident at an angle of 20° (see Fig. 3). Given the oblique incidence angle the cross-shore difference wave number is smaller resulting in slightly longer wave groups and a weaker response in both the infragravity surface elevation and cross-shore velocity response (compare left panels of Fig. 3 with Fig. 2). Although the equilibrium solution for obliquely incident sea-swell waves given by Reniers et al. (2002) is significantly smaller compared with the normally incident wave groups (compare the right panels in Figs. 2 and 3) it generally still overestimates the WGF infragravity wave amplitude. Comparing the IEM-predictions with the IAM results shows a good comparison for both the bi-phase and amplitude evolution (right panels A and C in Fig. 3). Excluding the obliqueness of the WGF infragravity wave results in an overprediction of the WGF infragravity wave height (compare with green line in right Panel A).

Analogous to Herbers and Burton (1997) the WGF infragravity amplitude at 4 m water depth is compared for a range in difference

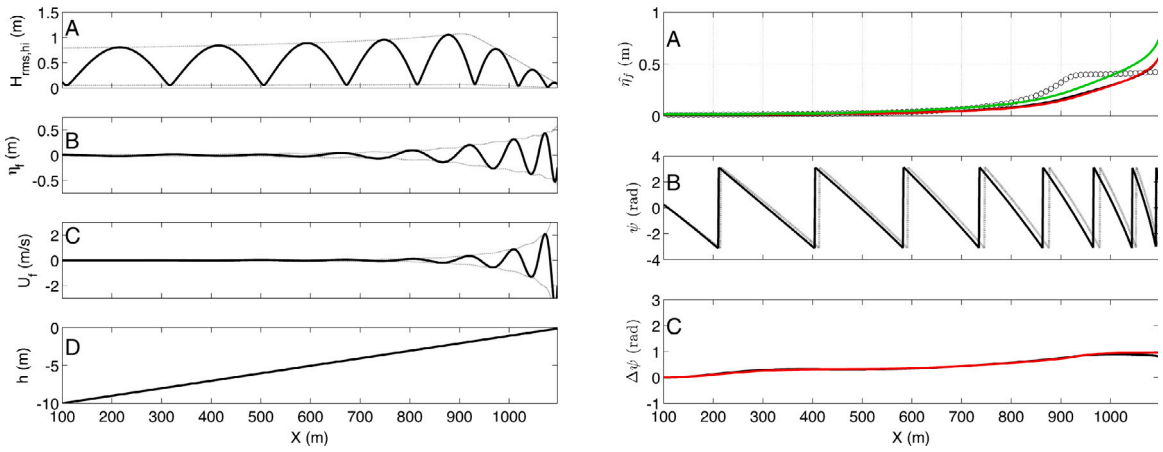

Fig. 3. Left panels: IAM predictions for an obliquely incident bi-chromatic wave train with frequency difference of 0.04 Hz and a deep water difference angle of 20°. Panel A: Snapshot of wave-group varying wave height (solid line) and corresponding envelope (dashed line). Panel B: Snapshot of concurrent WGF infragravity surface elevation (solid line) and corresponding envelope (dashed lines). Panel C: Similar but for the cross-shore infragravity velocity. Panel D: Corresponding bed elevation. Right panels: Panel A: IAM-predicted (thick black line) and IEM-predicted (thick red line) WGF infragravity wave amplitude. Equilibrium solution of Longuet-Higgins and Stewart (1964) given by the squares. IEM-predictions without taking obliqueness of infragravity waves into account (green line). Panel B: IAM-predicted phase of the wave group forcing (dashed) and the accompanying WGF infragravity wave (solid). Panel C: IAM-predicted bi-phase (black) compared with IEM-prediction (red).

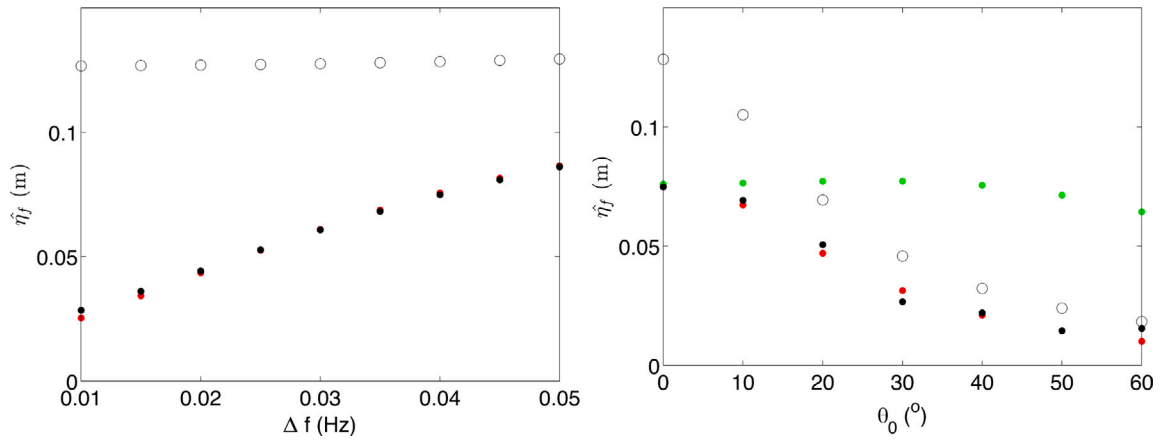

Fig. 4. Left panel: Forced infragravity amplitude at 4 m water depth predicted by IAM (black dots), IEM (red dots) and the equilibrium solution of Longuet-Higgins and Stewart (1964) for normally incident bi-chromatic waves as function of the difference frequency. Right panel: Forced infragravity amplitude at 4 m water depth predicted by IAM (black dots), IEM (red dots) and the equilibrium solution for obliquely incident bi-chromatic waves as function of the deep water difference angle. IEM-predictions without taking obliqueness of infragravity waves into account (green dots).

frequencies and directions. Computing the WGF infragravity amplitude for normally incident bi-chromatic wave for increasing difference frequencies, corresponding to subset 1 in Table 2, shows a gradual increase in both the IAM and IEM results (left panel of Fig. 4). The largest difference with the equilibrium solution occurs for the smallest difference frequency, consistent with the results obtained by Battjes et al. (2004). Keeping the difference frequency at 0.04 Hz but gradually increasing the deep water spreading angles, corresponding to subset 2 in Table 2, shows a significant decay in the predicted WGF infragravity amplitude at 4 m water depth consistent with the numerical results of Herbers and Burton (1997) (compare right panel in Fig. 4 with their Figs. 2a and 3a). The mismatch with the equilibrium solution decreases with increasing directional spreading. Overall the difference between the IAM and IEM predicted amplitudes at 4 m depth are small. Excluding the directional effects in estimating the WGF infragravity response results in a clear overestimation (compare with green dots in the right panel of Fig. 4).

3.2. Laboratory validation

The following describes the first part of the validation of the WGF infragravity predictions with SWAN for unidirectional random waves. Model simulations use a constant cross-shore grid spacing of 2.5 m, a 0.05 Hz–0.3 Hz frequency range for the sea-swell waves and a 0.01 Hz-0.04 Hz frequency range for the infragravity waves, both with a 0.01 Hz frequency resolution and 2 degree directional resolution. The normally incident waves are represented by a very narrow banded directional spectrum with a directional spreading of O(3)°. Both the wave breaking parameter γ_b and the reflection coefficient r_c are used as calibration coefficients.

Starting with test 1C0102 corresponding to swell conditions (see Table 1). The swell wave height prediction with $\gamma_b = 0.5$ closely matches the observations with the onset of breaking at the bar crest, subsequent cessation in the trough and additional breaking close to shore (see left panel A of Fig. 5) resulting a mean rms error of less than 0.02 m (see Table 3). The computed infragravity response shows a gradual increase in the total wave height consistent with the observations (left Panel B of Fig. 5) with the largest mismatch close to shore. Both the reflected and WGF infragravity wave height compare favorably with

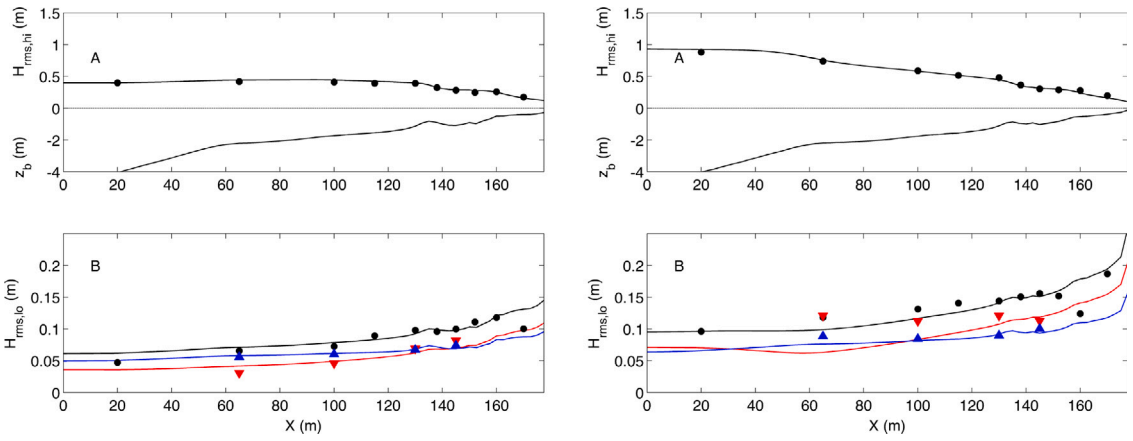

Fig. 5. Left panels: Wave transformation for test 1C0102. Panel A: Predicted (solid black line) and measured (black dots) root mean square swell wave height. Bottom profile given as a reference. Panel B. Predicted total (black), WGF (red) and reflected (blue) root mean square infragravity wave height. Measurements are indicated by the co-colored markers. Right Panels: Similar but for test 2B0506.

Table 3
Error statistics of the sea-swell and infragravity transformation for the LIP11D laboratory experiments given in Table 1.

LIP11D Test	1C0102	2B0506	2A0102
γ_b	0.5	0.6	0.6
r_c	0.89	0.8	0.92
$\epsilon(H_{rms,hi})$ (cm)	2.0	2.5	2.7
b($H_{rms,hi}$) (cm)	1.1	−0.5	2.2
sci($H_{rms,hi}$)	0.06	0.05	0.06
$\epsilon(H_{rms,lo,c})$ (cm)	1.2	2.0	1.7
b($H_{rms,lo,c}$)	0.4	0.1	−0.1
sci($H_{rms,lo,c}$)	0.13	0.14	0.13
$\epsilon(H_{rms,lo,f})$ (cm)	0.9	3.3	2.5
b($H_{rms,lo,f}$)	−0.1	−2.4	−2.2
sci($H_{rms,lo,f}$)	0.23	0.25	0.27
$\epsilon(H_{rms,lo,r})$ (cm)	1.0	0.7	0.9
b($H_{rms,lo,r}$)	0.1	−0.5	−0.8
sci($H_{rms,lo,r}$)	0.16	0.07	0.10

the measurements showing a steeper increase for the WGF response compared with the reflected infragravity waves, consistent with the non-linear forcing by the wave groups and inverse shoaling respectively (Battjes et al., 2004). The accompanying rms error estimates are in the order of 1 cm (see Table 3).

The wave transformation for test 2B0506 corresponds to erosive sea conditions with an increased wave height and reduced wave period (see Table 1). The waves start breaking at the beginning of the sloping bed and continue breaking all the way to the shoreline. Model predictions obtained with a γ_b of 0.6 are consistent with the measurements with a mean rms error of less than 3 cm (see Table 3). The predicted total infragravity response shows an underprediction offshore of the bar crest and an overprediction onshore caused by the mismatch of the WGF infragravity wave height resulting in a rms error of O(2) cm. The steep increase in the WGF infragravity wave height observed in test 1C0102 is mostly absent consistent with the reduced modulation by wave breaking represented by Eq. (25). Similar results are obtained for test 1A0102 (not shown) with the error statistics summarized in Table 3 showing a favorable model performance to normally incident wave forcing.

3.3. Field validation

Next the infragravity response to directionally spread sea-swell waves is examined comparing SWAN predictions with field observations obtained at Duck, North Carolina.

Model simulations use a constant cross-shore grid spacing of 5 m, a 0.05 Hz–0.3 Hz frequency range for the sea-swell waves and a 0.01 Hz–0.04 Hz frequency range for the infragravity waves, both with a 0.01 Hz frequency resolution and 10 degree directional resolution. The wave breaking parameter γ_b is used as a calibration parameter and the reflection coefficient r_c is set to one. The model is forced with the measured 3-hourly frequency-directional spectra. Daily surveys of the bathymetry are used to construct the profile at the instrument array. The conditions during Oct15 at 10 pm are taken as an example. The bed profile on this day shows a typical sand bar located around $x = 700$ m and a trough around $x = 800$ m (panel C in Fig. 6). The frequency-directional spectrum is relatively narrow banded in frequency, with a peak frequency at 0.095 Hz, combined with a directionally broad distribution, with a peak direction of −20° with respect to the shore normal (right panel in Fig. 6). The corresponding offshore root mean square wave height is 0.55 m with a tidal elevation of −0.3 m with respect to mean sea level.

The SWAN-predicted sea-swell wave height transformation, obtained with Eq. (21), shows a good match with the observations with wave breaking on the bar and near the shore line. The corresponding WGF infragravity spectrum, given by Eq. (29), is integrated over the infragravity frequency band, (0.01 Hz $\leq \Delta f \leq 0.04$ Hz), showing a strong increase with decreasing depth (panel A) consistent with the benchmark testing. The directional spreading of the WGF infragravity is restricted to incident wave angles only, i.e. ($-90° < \theta < 90°$). Offshore, the mean WGF direction aligns with the sea-swell waves of approximately −20° (right panel of Fig. 6) gradually moving towards the shore normal as the sea-swell waves refract with decreasing depth. Full reflection of the WGF infragravity energy is imposed at a water depth of 0.1 m. The reflected infragravity wave variance, computed with Eq. (34), shows a much broader directional distribution with a weak depth-dependent decay consistent with inverse shoaling and refraction. Refractive trapping is apparent at the shore line and over the bar (Bryan et al., 1998; Rijnsdorp et al., 2015), with reflected infragravity energy present at onshore wave directions.

Further integrating the WGF-infragravity spectrum over the directions yields the SWAN-predicted WGF infragravity root mean square wave height (red line in panel D in Fig. 6). At the deepest sensor location, CM90 ($x \sim 540$) m (c.f. Fig. 1), the WGF predictions are close to the bispectrally estimated bound infragravity wave height, suggesting a near balance between the WGF forcing and the accompanying bound infragravity wave. Closer to the shore line the WGF infragravity wave height increases further, whereas the observed bound infragravity wave height decays, consistent with the release of the bound infragravity wave and subsequent regular shoaling as the wave group forcing reduces due to breaking. Including the contribution of

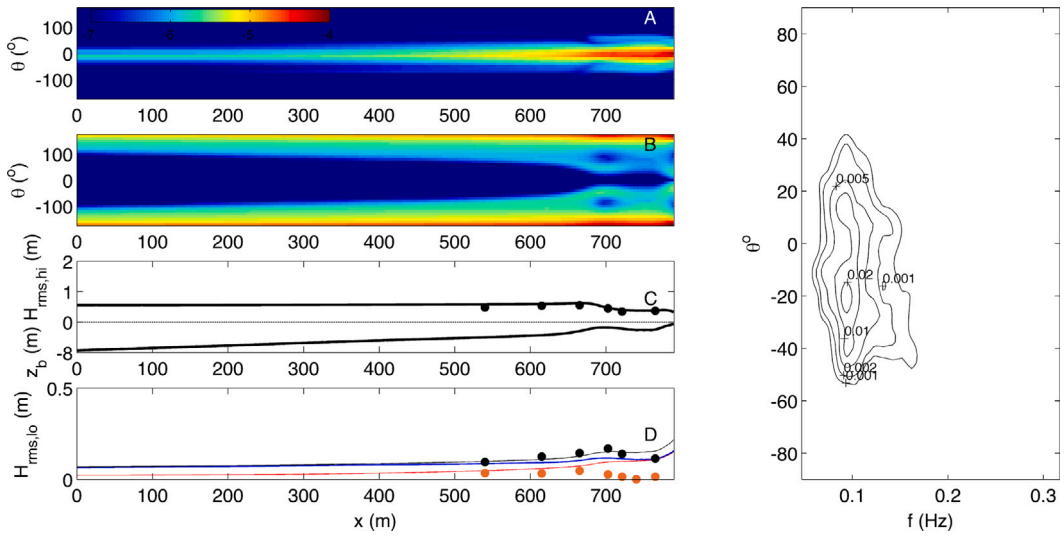

Fig. 6. Left panels: Wave transformation on October 15 at 10 pm. Panel A: Frequency-integrated WGF infragravity variance (logarithmic color scale in $m^2/°$). Panel B: Reflected infragravity variance. Panel C: $H_{rms,hi,c}$ (black line) compared with observations $H_{rms,hi,m}$ (black dots). Panel D: WGF $H_{rms,lo,f}$ (red line) compared with bound infragravity wave height (orange dots). Total predicted infragravity height $H_{rms,lo,c}$ (black line) compared with observations of $H_{rms,lo,c}$ (black dots). Reflected $H_{rms,lo,r}$ given as a reference (blue line). Right panel: Sea-swell frequency-directional spectrum at FRF 8-m array for October 15 at 10 pm. Direction θ is with respect to the shore normal. (For interpretation of the references to color in this figure legend, the reader is referred to the web version of this article.)

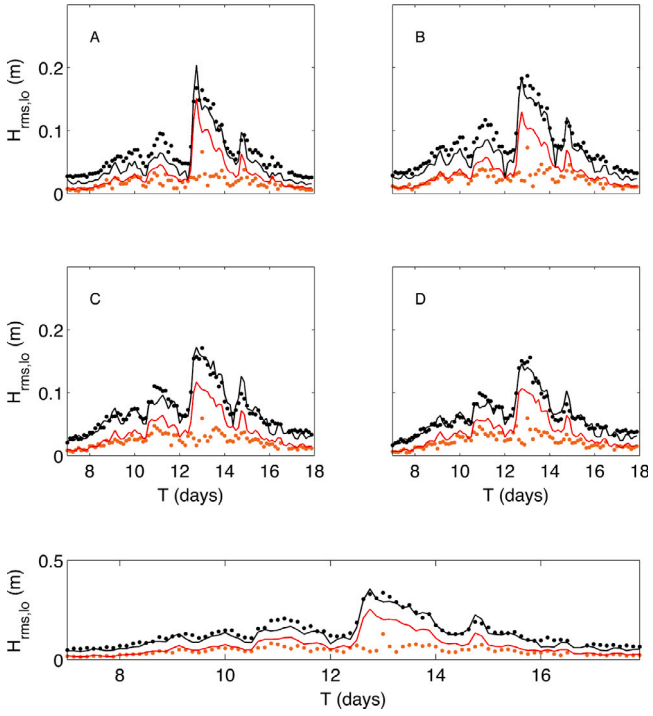

Fig. 7. Infragravity wave conditions at CM90 (see Fig. 1 for the location). Predicted total (black) and WGF (red) infragravity wave height compared with observations of total (black markers) and bound (orange markers) infragravity wave heights respectively at frequencies 0.01 Hz (Panel A), 0.02 Hz (panel B), 0.03 Hz (panel C) and 0.04 Hz (panel D) with a 0.01 Hz frequency bandwidth. Bottom panel: Corresponding frequency-integrated, 0.01 Hz–0.04 Hz, infragravity wave heights.

the reflected infragravity waves shows a good match with the measured total infragravity wave height, especially for the deeper sensor locations (black line in panel D).

The frequency-dependent infragravity response for all three-hourly predictions at location CM90 is examined next. To that end the predicted infragravity wave height for a 0.01 Hz frequency bandwidth ranging from 0.01 Hz to 0.04 Hz is compared with the observations. On average the total infragravity wave height in the higher infragravity

Table 4
Error statistics for the predicted infragravity conditions at CM90 for the total $H_{rms_{1}o_{c}}$ for a range in frequency bands corresponding to Fig. 7.

f (Hz)	$\epsilon(H_{rms_{1}o_{c}})$ (cm)	b($H_{rms_{1}o_{c}}$) (cm)	sci($H_{rms_{1}o_{c}}$)
0.01 Hz	1.6	−1.3	0.26
0.02 Hz	1.7	−1.4	0.21
0.03 Hz	1.1	−0.1	0.15
0.04 Hz	0.9	−0.2	0.14
0.01–0.04 Hz	2.2	−1.4	0.16

frequencies, $f \geq 0.03$ Hz, is well predicted by the model (panels C and D of Fig. 7) with an ϵ of O(1) cm and a scatter index SCi of O(0.15) (Table 4). For the lower infragravity frequencies, $f \leq 0.02$ Hz, the total infragravity wave height is typically underestimated during moderate sea-swell conditions (panels A and B of Fig. 7) resulting in a bias of approximately 1.5 cm and an increase in SCi to O(0.25) (Table 4). The predicted WGF-infragravity wave height compares well with the observations for all frequency bands, provided the sea-swell forcing is mild. During storm conditions the WGF-infragravity wave height exceeds the observed bound infragravity wave height consistent with the release and subsequent regular shoaling as observed for Oct 15 at 10 pm (Panel D in Fig. 6). Fully integrating the three-hourly infragravity frequency spectra shows a good match with the observations for the total infragravity wave height (lower panel in Fig. 7) with a rms-error of O(2) cm, with an underprediction during moderate conditions due to the diminished low frequency response (panels A and B in Fig. 7) resulting in a bias of −1.4 cm with an overall SCi of 0.16 (Table 4).

The model performance at the instrument locations closer to shore is considered next (see Fig. 1 for the locations). The frequency dependent results show significant scatter around the optimal fit corresponding to the diagonals in the left panels of Fig. 8. The mismatch with the observations seems to alternate between over/underpredictions for a given frequency band depending on the location of the instrument, consistent with the presence of nodes and anti-nodes in the surface elevation. This results in a small bias but a significantly increased scatter compared to the results obtained at CM90 (compare Tables 4 and 5). This mismatch is reduced by integrating over the full infragravity spectrum (right panel in Fig. 8) resulting in an overall root mean square error of O(4) cm and a scatter index of 0.22 (see Table 5).

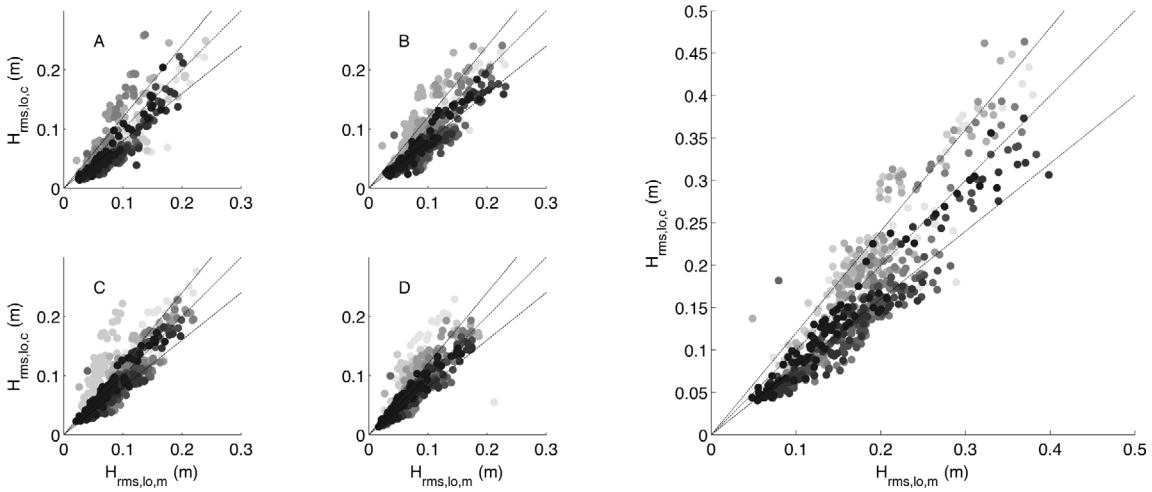

Fig. 8. Comparison of the predicted and measured total infragravity wave height at all sensor locations. Gray scale corresponds to the distance from the shore line (where the black dots correspond to CM90). Results are shown for the individual frequency bands of 0.01, 0.02, 0.03 0.04 Hz with a band width of 0.01 Hz in panels A, B, C and D respectively and the total infragravity band from 0.01–0.04 Hz in the larger panel on the right.

Table 5
Error statistics for the predicted infragravity conditions at all sensors combined for the total $H_{rms_{lo_c}}$ for a range in frequency bands corresponding to Fig. 8.

F (Hz)	$\epsilon(H_{rms_{lo_c}})$ (cm)	b($H_{rms_{lo_c}}$) (cm)	sci($H_{rms_{lo_c}}$)
0.01 Hz	2.7	−1.5	0.35
0.02 Hz	2.7	−1.0	0.29
0.03 Hz	2.7	0.2	0.30
0.04 Hz	2.3	0.1	0.29
0.01–0.04 Hz	3.9	−1.1	0.22

4. Discussion

In the computations phase locking between the WGF and reflected infragravity energy is absent (Eq. (36)). This is expected to hold further away from the shore line but not close to the reflection point (Guza and Thornton, 1985). This inhibits a proper comparison with the observations of the total infragravity wave height closer to the water line using Eq. (36). For normally incident regular infragravity waves with radial frequency ω the expected standing surface elevation amplitude, A, is given by:

$$A(\omega, X) = A(\omega)|_{X=0} \cos\left(\int_{X=0}^{X} k(X)dX\right)$$
$$\simeq A|_{X=0} \cos\left(\int_{X=0}^{X} \frac{\omega}{\sqrt{gh(X)}}dX\right) \quad (44)$$

with X starting at the reflection point being positive offshore. This approach assumes that the infragravity waves close to shore have been released and behave as free infragravity waves. The cross-shore structure within a certain frequency bandwidth can then be approximated by integrating Eq. (44) over the appropriate frequencies and scaling with the sum of the predicted incoming, $H_{rms,lo,f}$ and reflected, $H_{rms,lo,r}$, infragravity wave heights for that frequency bandwidth. Applying this to LIP11D test 1C0102 for a frequency bandwidth of 0.01 Hz shows that the cross-shore variability in the observations can be partly explained by the underlying standing wave patterns (left panels of Fig. 9).

Integrating over the full infragravity frequency range from 0.01–0.04 Hz the predicted total infragravity wave height, $H_{rms,lo,c}$, shows an improved match with the observations close to shore. This holds for all tests (right panels in Fig. 9). Around $x = 100$ m the nodal structure is mostly absent and Eq. (36) is valid. This means that for the offshore sensors in both the laboratory and field experiments Eq. (36) is expected to hold, but that close to shore the predicted results for the total infragravity wave height should be interpreted with care (refer to Guza and Thornton (1985) for improved estimates of standing infragravity wave patterns). Note that applying the same method for the DELILAH field experiment is not straightforward as the cross-shore wave number now not only depends on the infragravity incidence angle of both the incoming and outgoing infragravity waves but also the refractive trapping that is present (panel B in Fig. 6).

Model predictions for DELILAH typically demonstrate an underestimation of the energy in the lower infragravity frequency bins (panels A and B in Fig. 7 and Tables 4 and 5), especially at times of moderate sea-swell conditions. In the current approach it is assumed that the incoming infragravity energy is in equilibrium with the directionally spread sea-swell forcing at the FRF 8 m array. This ignores any free incident infragravity waves that originate from elsewhere (Bromirski et al., 2010; Ardhuin et al., 2014; Neale et al., 2015; Vrećica et al., 2019; Rijnsdorp et al., 2021). Ardhuin et al. (2014) use a empirical approach to obtain the outgoing infragravity waves at the coast as a boundary condition for their global infragravity modeling. By coupling with a regional model like SWAN, a potentially more accurate prediction can be made of the outgoing infragravity waves in both frequency distribution and direction. This two-way coupling is expected to lead to improved predictions of the incoming infragravity waves that can subsequently be used by other models to examine the coastal safety related to for instance beach and dune erosion as well overwash and breaching.

Model predictions have been performed without taking bed friction into account. This compensates partly for the omission in the radiation stress forcing related to the roller contribution as demonstrated by Reniers et al. (2002). Additional energy dissipation can occur by infragravity wave breaking within the swash zone (Henderson et al., 2006; Van Dongeren et al., 2007; Lin and Hwung, 2012; De Bakker et al., 2014). In the LIP11D laboratory cases this is represented with a reduced reflection coefficient ranging between 0.8 and 0.93 (Table 3. For the Delilah field experiment the reflection coefficient has been set to unity, although based on the work of Van Dongeren et al. (2007) a reduced reflection coefficient for the higher infragravity frequency bands is expected similar to what is observed in the laboratory experiment. Additional effects associated with the presence of an alongshore wave-driven current (Howd et al., 1992) and set-up have also not been taken into account, although the latter is expected to be less important provided the sea-swell wave height is predicted well (Reniers et al., 2002).

Additional model limitations are related to the underlying assumption of alongshore bathymetric uniformity. This limits the applicability to coasts that have only mild alongshore variations in the bathymetry

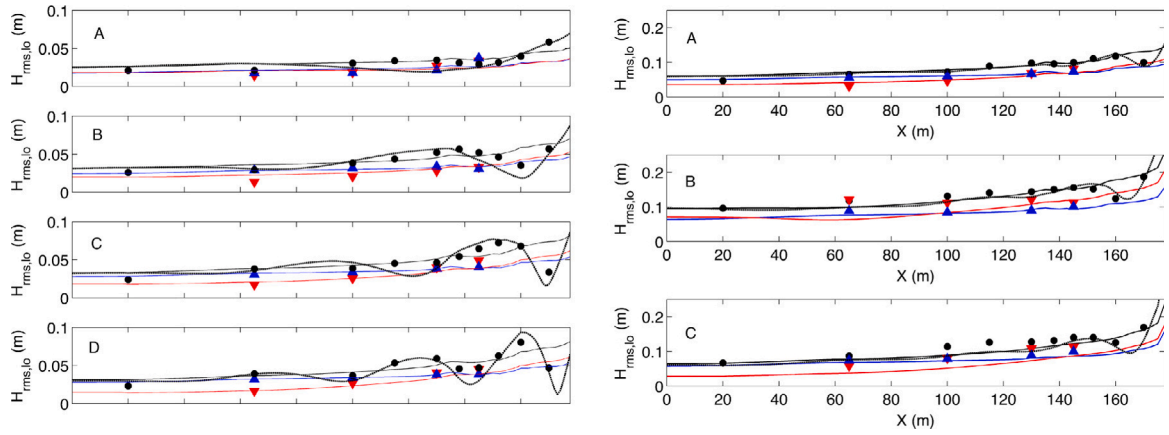

Fig. 9. Left panels: Infragravity wave heights for frequencies 0.01 Hz (panel A), 0.02 Hz (panel B), 0.03 Hz (panel C) and 0.04 Hz (panel D) with a 0.01 Hz bandwidth. Predicted (red line) and observed (red markers) WGF heights, predicted (blue line) and observed (blue markers) reflected wave heights and predicted total infragravity wave heights with (black dashed line) and without (black solid line) interference patterns and observations (black markers). Right panels: Similar but now for the frequency-integrated infragravity wave height for tests 1C0102 (panel A), 2B0506 (panel B) and 1A0102 (panel C).

and shore line position. To overcome this problem a more general description of the infragravity source term, S_{sb} and associated bi-phase $\Delta\psi$, is required taking into account 2D bathymetric variability (Janssen, 2006) but retaining the current computational efficiency allowing for realistic applications.

The modeled transfer of wave energy to the WGF infragravity wave is one-way, i.e. there is no equivalent loss of energy for the sea-swell waves forcing the infragravity response, nor is there a mechanism to extract energy from the infragravity waves and return it to the sea-swell waves (e.g. Thompson et al., 2006; Henderson et al., 2006; De Bakker et al., 2015). Additionally the effect of bore merging is absent (Sénéchal et al., 2001a; Tissier et al., 2015, 2017). As a result the representation of the infragravity dynamics in the inner surf and swash zone is limited. Finally, the release of the bound infragravity waves is represented by a reduction in the WGF depending on the fraction of breaking waves in Eq. (25). This approach takes into account the changes in the WGF forcing but does not account for the fact that the released infragravity waves subsequently propagate with $\sqrt{gh}$ instead of the group velocity c_g. In relatively shallow water, like the surfzones considered here, this is not a problem as both velocities are similar, but it does not work properly in case the infragravity waves enter a deeper tidal channel after passing over for instance a shallow shoal.

5. Conclusions

Wave Group Forcing of infragravity waves has been implemented in SWAN as a first step to predict the generation, propagation and evolution of infragravity waves at regional scales. The WGF is based on a description of the energy balance of infragravity waves forced by directionally spread random waves at an alongshore uniform coast. The subsequent extension of the infragravity energy balance has been verified with a benchmark comparison with the Infragravity Amplitude Model developed by Reniers et al. (2002) and shows a good match for both normally incident and obliquely incident wave group forcing. The subsequent implementation of the WGF in SWAN has been validated with both large-scale laboratory experiments and field observations. The laboratory experiments consist of normally incident random waves representing both accretive and erosive conditions. The field observations correspond to the WGF by a fully directional sea-swell spectrum. In both cases the SWAN infragravity predictions show a favorable match with observations provided the measurement location is not affected by the interference patterns created by the phase coupling of the incident and reflected infragravity waves. As a result the mismatch with the observed total infragravity wave height generally increases closer to shore although the specifics depend on the infragravity frequency band under consideration. The model application is restricted to alongshore uniform beaches with a mildly sloping beach profile. In these cases it can be used to provide the combined sea-swell and infragravity boundary conditions for more sophisticated, but computationally expensive, models at relatively shallow depths while reducing the error associated with the assumption of a local equilibrium between the WGF and the bound infragravity wave. This is deemed especially important during storm conditions that are used for coastal safety assessments as well as engineering studies for harbor designs to optimize access and minimize downtime.

CRediT authorship contribution statement

Ad Reniers: Conceptualization, Methodology, Validation, Writing – original draft. **Marcel Zijlema:** Software, Verification, Writing – review & editing.

Declaration of competing interest

The authors declare that they have no known competing financial interests or personal relationships that could have appeared to influence the work reported in this paper.

Acknowledgments

Data used in this study are provided by the Field Research Facility of the US Army Engineer Waterways Experiment Station's Coastal Engineering Research Centre. Accessibility and permission to use these data is appreciated very much. We also appreciate the discussions with Dr. Marion Tissier and Ir. Gal Akrish on the content of the work presented in this article.

Appendix A. Derivation of the bi-phase evolution for obliquely incident waves

The following is an extension of the work by Janssen et al. (2003) by including the alongshore component of the incident and infragravity waves at an alongshore uniform beach, consistent with the modeling approach of Reniers et al. (2002). This means that the WGF infragravity surface elevation is written as:

$$\eta_f(x,y,t) = \frac{1}{2}\hat{\eta}_f(x)\exp(i(-\Delta\omega t + \Delta k_y y)) + * \tag{A.1}$$

and the radiation stress forcing as:

$$S_{ij}(x,y,t) = \hat{S}_{ij}\exp(i\psi(x))\exp(i(-\Delta\omega t + \Delta k_y y)) + * \tag{A.2}$$

which upon substitution in the linearized long wave equation, Eq. (1), yields:

$$gh\frac{\partial^2\hat{\eta}_f}{\partial x^2}+g\frac{\partial h}{\partial x}\frac{\partial\hat{\eta}_f}{\partial x}+\Delta\omega^2\hat{\eta}_f-gh\Delta k_y^2\hat{\eta}_f= \tag{A.3}$$
$$-\frac{1}{\rho}\left(\frac{\partial^2\hat{S}_{xx}\exp\psi}{\partial x^2}+2i\Delta k_y\frac{\partial\hat{S}_{xy}\exp\psi}{\partial x}-\Delta k_y^2\hat{S}_{yy}\exp\psi\right)$$

Following Janssen et al. (2003) a slow cross-shore spatial scale is introduced:

$$X=\beta x \tag{A.4}$$

assuming that the changes in the water depth are small compared with the WGF infragravity wave length expressed by the scaling parameter β:

$$\beta=O\left(\frac{1}{\Delta k_x h}\frac{dh}{dx}\right) \tag{A.5}$$

Next the complex surface elevation amplitude is written as a combination of the slow spatial scale X and the faster phase changes at the group scale:

$$\hat{\eta}_f(X)=T(X)\exp(i\int_0^X\Delta k_x\beta^{-1}dX)=T(X)\exp(i\psi(X)) \tag{A.6}$$

that is substituted in the long wave equation, Eq. (A.3) where the different terms will be evaluated based on their relative contribution expressed by the scaling parameter β where the following identity is used:

$$\frac{\partial}{\partial x}=\beta\frac{\partial}{\partial X} \tag{A.7}$$

Starting with the first term on the lhs of Eq. (A.3) we obtain:

$$gh\frac{\partial^2\hat{\eta}_f}{\partial x^2}=gh\beta^2\frac{\partial^2\hat{\eta}_f}{\partial X^2}=gh\beta^2\left(\frac{\partial}{\partial X}\left(\frac{\partial T}{\partial X}\exp i\psi+i\beta^{-1}T\Delta k_x\exp i\psi\right)\right) \tag{A.8}$$
$$=gh\beta^2\left(\frac{\partial^2T}{\partial X^2}+i\beta^{-1}\Delta k_x\frac{\partial T}{\partial X}\right.$$
$$\left.+i\beta^{-1}T\frac{\partial\Delta k_x}{\partial X}+i\beta^{-1}\Delta k_x\frac{\partial T}{\partial X}-\beta^{-2}T\Delta k_x^2\right)\exp i\psi$$

followed by the second term gives:

$$g\frac{dh}{dx}\frac{\partial\hat{\eta}_f}{\partial x}=g\beta^2\frac{dh}{dX}\frac{\hat{\eta}_f}{\partial X}=\beta^2g\frac{dh}{dX}\left(\frac{dT}{dx}+i\beta^{-1}\Delta k_xT\right)\exp i\psi \tag{A.9}$$

the third term:

$$\Delta\omega^2\hat{\eta}_f=\Delta\omega^2T\exp i\psi \tag{A.10}$$

and finally the fourth term:

$$-gh\Delta k_y^2\hat{\eta}_f=-gh\Delta k_y^2T\exp i\psi \tag{A.11}$$

Collecting all the terms up to β, thus ignoring β^2 contributions, yields:

$$gh\Delta k_x^2\left(-\mu T+\frac{i\beta}{\Delta k_x}\left(2\frac{dT}{dX}+\frac{T}{\Delta k_x}\frac{d\Delta k_x}{dX}+\frac{T}{h}\frac{dh}{dX}\right)\right)\exp i\psi \tag{A.12}$$

where μ is the resonance mismatch:

$$\mu=\left(1-\frac{\Delta\omega^2-gh\Delta k_y^2}{gh\Delta k_x^2}\right) \tag{A.13}$$

Next the right hand side of Eq. (A.3) is evaluated. Starting with the first term on the r.h.s.:

$$\frac{\partial^2\hat{S}_{xx}\exp(i\psi)}{\partial x^2}=\beta^2\frac{\partial^2\hat{S}_{xx}\exp(i\psi)}{\partial X^2}= \tag{A.14}$$
$$\beta^2\left(\frac{d^2\hat{S}_{xx}}{dX^2}+2i\beta^{-1}\Delta k_x\frac{d\hat{S}_{xx}}{dX}+i\beta^{-1}\frac{d\Delta k_x}{dX}\hat{S}_{xx}-\beta^{-2}\Delta k_x^2\hat{S}_{xx}\right)\exp(i\Psi)$$

followed by the second term:

$$2i\Delta k_y\frac{\partial\hat{S}_{xy}exp(\psi)}{\partial x}=2\beta i\Delta k_y\frac{\partial\hat{S}_{xy}\exp(i\psi)}{\partial X}$$
$$=2\beta i\Delta k_y\left(\frac{d\hat{S}_{xy}}{dX}+i\beta^{-1}\Delta k_x\hat{S}_{xy}\right)\exp(i\psi) \tag{A.15}$$

and lastly the third term:

$$-\Delta k_y^2\hat{S}_{yy}exp(i\psi)=-\Delta k_y^2\hat{S}_{yy}exp(i\psi) \tag{A.16}$$

Again collecting all the terms of the rhs up to order β gives:

$$gh\Delta k_x^2\left(\frac{2i\beta}{gh\Delta k_x}\frac{d\hat{S}_{xx}}{dX}+\frac{i\beta\hat{S}_{xx}}{gh\Delta k_x^2}\frac{d\Delta k_x}{dX}-\frac{\hat{S}_{xx}}{gh}\right.$$
$$\left.+\frac{2i\beta\Delta k_y}{gh\Delta k_x^2}\frac{d\hat{S}_{xy}}{dX}-\frac{2\Delta k_y\hat{S}_{xy}}{gh\Delta k_x}-\frac{\Delta k_y^2\hat{S}_{yy}}{gh\Delta k_x^2}\right)\exp(i\psi) \tag{A.17}$$

Returning to physical spatial variable x and equating to the lhs with the rhs dividing both with $gh\Delta k_x^2$:

$$\left(-\mu T+\frac{i}{\Delta k_x}\left(2\frac{dT}{dx}+\frac{T}{\Delta k_x}\frac{d\Delta k_x}{dx}+\frac{T}{h}\frac{dh}{dx}\right)\right)\exp i\psi= \tag{A.18}$$
$$\frac{1}{\rho}\left(-\frac{\hat{S}_{xx}}{gh}-\frac{2\Delta k_y\hat{S}_{xy}}{gh\Delta k_x}-\frac{\Delta k_y^2\hat{S}_{yy}}{gh\Delta k_x^2}+\frac{2i}{gh\Delta k_x}\frac{d\hat{S}_{xx}}{dx}\right.$$
$$\left.+\frac{i\hat{S}_{xx}}{gh\Delta k_x^2}\frac{d\Delta k_x}{dx}+\frac{2i\Delta k_y}{gh\Delta k_x^2}\frac{d\hat{S}_{xy}}{dx}\right)\exp(i\psi)$$

This can be simplified by making use of the following expressions:

$$c_g=\frac{\Delta\omega}{\Delta k} \tag{A.19}$$

and:

$$\frac{1}{\Delta k_x}\frac{d\Delta k_x}{dx}=\frac{1}{\Delta k\cos\theta_f}\frac{d}{dx}\frac{\Delta\omega\cos\theta_f}{c_g}=\frac{1}{\Delta k\cos\theta_f}$$
$$\times\left(\frac{-\Delta\omega\cos\theta_f}{c_g^2}\frac{dc_g}{dx}+\frac{\Delta\omega}{c_g}\frac{d\cos\theta_f}{dx}\right)= \tag{A.20}$$
$$\left(\frac{-1}{c_g}\frac{dc_g}{dx}+\frac{1}{\cos\theta_f}\frac{d\cos\theta_f}{dx}\right)=-\frac{\cos\theta_f}{c_g}\frac{d\frac{c_g}{\cos\theta_f}}{dx}$$

and multiplying with $\Delta k_x/2/i$ gives (dropping $\exp i\psi$):

$$\frac{dT}{dx}+\frac{i\mu\Delta k_x}{2}T=\left(\frac{\cos\theta_f}{2c_g}\frac{d\frac{c_g}{\cos\theta_f}}{dx}-\frac{1}{2h}\frac{dh}{dx}\right)T+\frac{\hat{S}_{xx}}{2\rho gh}$$
$$\times\left(i\Delta k_x+\frac{2}{\hat{S}_{xx}}\frac{d\hat{S}_{xx}}{dx}-\frac{\cos\theta_f}{c_g}\frac{d\frac{c_g}{\cos\theta_f}}{dx}\right)+ \tag{A.21}$$
$$\frac{\hat{S}_{xy}}{\rho gh}\left(i\Delta k_y+\frac{\Delta k_y}{\Delta k_x}\frac{1}{\hat{S}_{xy}}\frac{d\hat{S}_{xy}}{dx}\right)+\frac{\hat{S}_{yy}}{\rho gh}\left(\frac{\Delta k_y^2}{\Delta k_x}\right)$$

where μ is given by Eq. (17).

In the case of normally incident waves, Δk_y and $\cos\theta_f$ both equal 0 and Eq. (23) of Janssen et al. (2003) is retrieved. Following Janssen et al. (2003) the equation is written as a function of phase difference between the WGF infragravity wave, $|T|=|\eta_f|$, and the (negative) radiation stress forcing corresponding to the bi-phase, $\Delta\psi$:

$$\frac{d|\eta_f|}{dx}+i|\eta_f|\frac{d\Delta\psi}{dx}+\frac{i\mu\Delta k_x}{2}|\eta_f|=\left(\frac{\cos\theta_f}{2c_g}\frac{d\frac{c_g}{\cos\theta_f}}{dx}-\frac{1}{2h}\frac{dh}{dx}\right)|\eta_f|+ \tag{A.22}$$
$$\frac{\hat{S}_{xx}}{2\rho gh}(\cos\Delta\psi+i\sin\Delta\psi)\left(i\Delta k_x+\frac{2}{\hat{S}_{xx}}\frac{d\hat{S}_{xx}}{dx}-\frac{\cos\theta_f}{c_g}\frac{d\frac{c_g}{\cos\theta_f}}{dx}\right)+$$
$$\frac{\hat{S}_{xy}}{\rho gh}(\cos\Delta\psi+i\sin\Delta\psi)\left(i\Delta k_y+\frac{\Delta k_y}{\Delta k_x}\frac{1}{\hat{S}_{xy}}\frac{d\hat{S}_{xy}}{dx}\right)$$
$$+\frac{\hat{S}_{yy}}{\rho gh}(\cos\Delta\psi+i\sin\Delta\psi)\left(\frac{\Delta k_y^2}{\Delta k_x}\right)$$

Collecting the imaginary contributions the evolution equation for the bi-phase is obtained:

$$\frac{d\Delta\psi}{dx} = -\frac{\mu\Delta k_x}{2} + \frac{\hat{S}_{xx}}{2\rho g h|\eta_f|} \times \left(\Delta k_x \cos\Delta\psi - \left(\frac{2}{\hat{S}_{xx}} \frac{d\hat{S}_{xx}}{dx} - \frac{\cos\theta_f}{c_g} \frac{d\frac{c_g}{\cos\theta_f}}{dx} \sin\Delta\psi \right) \right) + \frac{\hat{S}_{xy}}{\rho g h|\eta_f|} \left(\Delta k_y \cos\Delta\psi + \frac{\Delta k_y}{\Delta k_x} \frac{1}{\hat{S}_{xy}} \frac{d\hat{S}_{xy}}{dx} \sin\Delta\psi \right) - \frac{\hat{S}_{yy}}{\rho g h|\eta_f|} \left(\frac{\Delta k_y^2}{\Delta k_x} \sin\Delta\psi \right) \quad \text{(A.23)}$$

which reduces to the solution given by Janssen et al. (2003) for normally incident waves, i.e. their Eq. (25). The equilibrium solution for a horizontal bed with $\Delta\psi = 0$ yields:

$$-\frac{\Delta k_{x,0}\mu_0}{2} + \frac{\hat{S}_{xx,0}}{2\rho g h_0|\hat{\eta}_{f,0}|}\Delta k_{x,0} + \frac{\hat{S}_{xy,0}}{\rho g h_0|\hat{\eta}_{f,0}|}\Delta k_y = 0 \quad \text{(A.24)}$$

from which it follows that:

$$|\hat{\eta}_{f,0}| = \frac{\hat{S}_{xx,0} + 2\hat{S}_{xy,0}\frac{\Delta k_y}{\Delta k_{x,0}}}{\mu_0 \rho g h_0} \quad \text{(A.25)}$$

where the subscript 0 refers to the offshore conditions.

Appendix B. Finite difference equations

Writing the coupled differential equations for the bound infragravity energy flux and the bi-phase yields for Eq. (15) :

$$F_{x,j+1} = F_{x,j} + \Delta x \left(\frac{1}{2}\Delta k_{x,j+1}\hat{U}_{f,x,j}\hat{S}_{xx,j+1}\sin\Delta\psi_j + \frac{1}{2}\Delta k_{y,j+1}\hat{U}_{f,y,j}\hat{S}_{xy,j+1}\sin\Delta\psi_j \right) \quad \text{(B.1)}$$

and for Eq. (16):

$$\Delta\psi_{j+1} = \Delta\psi_j - \Delta x \left(\frac{\Delta k_{x,j+1}\mu_{j+1}}{2} \right) - \frac{\hat{S}_{xx,j+1}}{2\rho g h_{j+1}|\hat{\eta}_{f,j}|} \left(\Delta x \Delta k_{x,j+1}\cos\Delta\psi_j - \left(2\frac{\hat{S}_{xx,j+1} - \hat{S}_{xx,j}}{\hat{S}_{xx,j+1}} - \frac{c_{g,j+1} - c_{g,j}}{c_{g,j+1}} \right) \sin\Delta\psi_j \right) + \frac{\hat{S}_{xy,j+1}}{\rho g h_{j+1}|\hat{\eta}_{f,j}|} \left(\Delta x \Delta k_y \cos\Delta\psi_j - \frac{\Delta k_y}{\Delta k_{x,j+1}} \left(\frac{\hat{S}_{xy,j+1} - \hat{S}_{xy,j}}{\hat{S}_{xy,j+1}} \right) \sin\Delta\psi_j \right) - \frac{\Delta x \hat{S}_{yy,j+1}}{2\rho g h_{j+1}|\hat{\eta}_{f,j}|} \frac{\Delta k_y^2}{\Delta k_{x,j+1}} sin(\Delta\psi_j) \quad \text{(B.2)}$$

respectively, where Δx is the cross-shore grid spacing. Here, a uniform grid is $j\Delta x$, $j = 0, 1, ..N$ is employed where N is the number of grid cells. Point $j = 0$ indicates the offshore boundary where boundary condition Eq. (19) and $\Delta\psi = 0$ are imposed for the WGF-infragravity energy flux and bi-phase respectively. Cross-shore-integration yields the bound long wave energy, amplitude and bi-phase that can be compared with the IAM results for obliquely incident bi-chromatic waves.

References

Arcilla, A.S., Roelvink, J.A., OConnor, B.A., Reniers, A., Jimenez, J.A., 1994. The delta flume 93 experiment. In: Coastal Dynamics 94 (Bareclona, Spain), pp. 488-502.

Ardhuin, F., Rawat, A., Aucan, J., 2014. A numerical model for free infragravity waves: definition and validation at regional and global scales. Ocean Model. 77, 20–32.

Baldock, T.E., Holmes, P., Bunker, S., Van Weert, P., 1998. Cross-shore hydrodynamics within an unsaturated surf zone. Coast. Eng. 34, 173–196.

Battjes, J.A., Bakkenes, H.J., van Dongeren, A.R., 2004. Shoaling of subharmonic gravity waves. J. Geophys. Res. 109, C02009. http://dx.doi.org/10.1029/2003JC001863.

Battjes, J.A., Janssen, J.P.F.M., 1978. Energy loss and set-up due to breaking of random waves. In: Edge, B. (Ed.), Proceedings of the 16th International Conference on Coastal Engineering. Am. Soc. of Civ. Eng., Reston, Va, pp. 569–587.

Benoit, M., Marcos, F., Becq, F., 1996. Development of a third generation shallow water wave model with unstructured spatial meshing. In: Proc. 25th International Conference on Coastal Engineering (ICCE'1996), Orlando, USA, pp. 465–478.

Bertin, X., et al., 2018. Infragravity waves: From driving mechanisms to impacts. Earth-Sci. Rev. 177, 774–799. http://dx.doi.org/10.1016/j.earscirev.2018.01.002.

Biesel, F., 1952. Equations generales au second ordre de la houle irreguleiere. La Houille Blanch 371–376.

Booij, N., Ris, R.C., Holthuijsen, L.H., 1999. A third-generation wave model for coastal regions, 1. Model description and validation. J. Geophys. Res. 104, 7, 649–7, 666.

Bromirski, P.D., Sergienko, O.V., MacAyeal, D.R., 2010. Transoceanic infragravity waves impacting antarctic ice shelves. Geophys. Res. Lett. 37.

Bryan, K.R., Howd, P.A., Bowen, A.J., 1998. Field observations of bar-trapped edge waves. J. Geophys. Res. 103, 1285–1305.

De Bakker, A.T.M., Herbers, T.H.C., Smit, P.B., Tissier, M.F.S., Ruessink, B.G., 2015. Nonlinear infragravity-wave interactions on a gently sloping laboratory beach. J. Phys. Oceanogr. 45, 589–605. http://dx.doi.org/10.1175/JPO-D-14-0186.1.

De Bakker, A.T.M., Tissier, M.F.S., Ruessink, B.G., 2014. Shoreline dissipation of infragravity waves. Cont. Shelf Res. 72, 73–82. http://dx.doi.org/10.1016/j.csr.2013.11.013.

Eldeberky, Y., Battjes, J.A., 1995. Parameterisation of triad interactions in wave energy models. In: Proc. Coastal Dynamics Conf. '95, Gdansk, Poland, pp. 140–148.

Elgar, S., Guza, R.T., 1985. Observations of bispectra of shoaling surface gravity waves. J. Fluid Mech. 161, 425–448.

Fiedler, J.W., Smit, Pieter B., Brodie, Katherine L., McNinch, Jesse, Guza, R.T., 2019. The offshore boundary condition in surf zone modeling. Coast. Eng. 143, 12–20. http://dx.doi.org/10.1016/j.coastaleng.2018.10.014.

Guza, R.T., Feddersen, F., 2012. Effect of wave frequency and directional spread on shoreline runup. Geophys. Res. Lett. 39, L11607. http://dx.doi.org/10.1029/2012GL051959.

Guza, R.T., Thonrnton, E.B., Holman, R.A., 1984. Swash on steep and shallow beaches. In: Proc. of the 19th Int. Conf. Coastal Eng.. ASCE, pp. 708–723.

Guza, R.T., Thornton, E.B., 1982. Swash oscillations on a natural beach. J. Geophys. Res. 87 (C1), 483–491.

Guza, R.T., Thornton, E.B., 1985. Observations of surf beat. J. Geophys. Res. 87, 483–491.

Hasselmann, K., 1962. On the non-linear energy transfer in a gravity-wave spectrum part 1. General theory. J. Fluid Mech. 12, 481–500.

Hasselmann, S., Hasselmann, K., Janssen, P.A.E.M., et al., 1988. The WAM model - a third generation ocean wave prediction model. J. Phys. Oceanogr. 18 (12), 1775–1810.

Hasselmann, K., Munk, W., MacDonald, G., 1963. Bispectra of ocean waves. In: Rosenblatt, M. (Ed.), Time Series Analysis. John Wiley, New York.

Henderson, S.M., Guza, R.T., Elgar, S., Herbers, T.H.C., Bowen, A.J., 2006. Nonlinear generation and loss of infragravity wave energy. J. Geophys. Res. 111, C12007. http://dx.doi.org/10.1029/2006JC003539.

Herbers, T.H.C., Burton, M.C., 1997. Nonlinear shoaling of directionally spread waves on a beach. J. Geophys. Res. 102, 21101–21114.

Herbers, T.H.C., Elgar, S., Guza, R.T., 1994. Infragravity-frequency (0.005–0.05 hz) motions on the shelf, part I : Forced waves. J. Phys. Oceanogr. 24, 917–927.

Herbers, T.H.C., Elgar, S., Guza, R.T., 1995. Generation and propagation of infragravity waves. J. Geophys. Res. 100, 24863–24872.

Holman, R.A., 1981. Infragravity energy in the surf zone. J. Geophys. Res. 86, 6442–6450.

Howd, P.A., Bowen, A.J., Holman, R.A., 1992. Edge waves in the presence of strong longshore currents. J. Geophys. Res. 97, 11357–11371.

Janssen, T.T., 2006. Nonlinear Surface Waves over Topography (Ph.D. thesis). Technical University of Delft, The Netherlands.

Janssen, T.T., Battjes, J.A., van Dongeren, A.R., 2003. Long waves induced by short wave groups over a sloping bottom. J. Geophys. Res. 108 (C8), 3252. http://dx.doi.org/10.1029/2002JC001515.

Lin, Y.-H., Hwung, H.-H., 2012. Infra-gravity wave generation by the shoaling wave groups over beaches. China Ocean Eng. 26, 1–18.

Longuet-Higgins, M.S., Stewart, R.W., 1962. Radiation stress and mass transport in gravity waves with applications to 'surf-beats'. J. Fluid. Mech. 8, 565–583.

Longuet-Higgins, M.S., Stewart, R.W., 1964. Radiation stresses in water waves. a physical discussion, with applications. Deep Sea Res. 11, 529–562.

Madsen, P.A., Sorensen, O.R., 1993. Bound waves and triad interactions in shallow water. J. Ocean Eng. 20 (4), 359–388.

McCall, R., Van Thiel de Vries, J.S.M., Plant, N., Van Dongeren, A.R., Roelvink, J.A., Thompson, D., Reniers, A., 2010. Two-dimensional time dependent hurricane overwash and erosion modeling at santa rosa island. Coast. Eng. 57, 668–683. http://dx.doi.org/10.1016/j.coastaleng.2010.02.006.

Mei, C.C., Benmoussa, C., 1984. Long waves induced by short wave groups over an uneven bottom. J. Fluid Mech. 139, 219–235.

Munk, W., 1949. Surf beat. Eos Trans. AGU 30, 849–854.

Neale, J., Harmon, N., Srokosz, M., 2015. Source regions and reflection of infragravity waves offshore of the U.S. Pacific northwest. J. Geophys. Res. 120, 1–18.

Phillips, O.M., 1977. The Dynamics of the Upper Ocean, second ed. Cambridge University Press, Cambridge-London-New York-Melbourne, p. 336.

Rawat, A., Ardhuin, F., Ballu, V., Crawford, W., Corela, C., Aucan, J., 2014. Infragravity waves across the oceans. Geophys. Res. Lett. 41, 7957–7963. http://dx.doi.org/10.1002/2014GL061604.2014GL061604.

Reniers, A.J.H.M., van Dongeren, A.R., Battjes, J.A., Thornton, E.B., 2002. Linear modelling of infragravity waves during delilah. J. Geophys. Res. 107, 3137. http://dx.doi.org/10.1029/2001JC001083.

Reniers, A.J.H.M., Groenewegen, M.J., Ewans, K.C., Masterton, S., Stelling, G.S., Meek, J., 2010. Estimations of infragravity waves at intermediate depth. Coast. Eng. 57, 52–61.

Rijnsdorp, D.P., Reniers, A.J.H.M., Zijlema, M., 2021. Free infragravity waves in the north sea. J. Geophys. Res. 126 (8), http://dx.doi.org/10.1029/2021JC017368.

Rijnsdorp, D.P., Ruessink, B.G., Zijlema, M., 2015. Infragravity-wave dynamics in a barred coastal region, a numerical study. J. Geophys. Res. 120 (6), 4068–4089. http://dx.doi.org/10.1002/2014JC010450.

Roelvink, J.A., Reniers, A.J.H.M., 1994. LIP11D Delta Flume Experiments. Data report H2130, WL/Delft Hydraulics, The Netherlands.

Roelvink, D., Reniers, A., van Dongeren, A., van Thiel de Vries, J., McCall, R., Lescinski, J., 2007. Modelling storm impacts on beaches, dunes and barrier islands. Coast. Eng. 56, 1133–1152.

Ruessink, B.G., 1998a. Bound and free infragravity waves in the nearshore zone under breaking and nonbreaking conditions. J. Geophys. Res. 103, 12.795–12.805.

Ruessink, B.G., 1998b. The temporal and spatial variability of infragravity energy in a barred nearshore zone. Cont. Shelf Res. 18, 585–605.

Ruggiero, P., Holman, R.A., Beach, R.A., 2004. Wave run-up on a high-energy dissipative beach. J. Geophys. Res. 109 (C06025).

Schäffer, H.A., 1993. Infragravity waves induced by short wave groups. J. Fluid Mech. 247, 551–588.

Schäffer, H.A., Svendsen, I.A., 1988. Surf beat generation on a mild-slope beach. In: Proc. of the 21st International Conf. Coastal Eng.. Torremolinos, Spain, http://dx.doi.org/10.9753/icce.v21.79.

Sénéchal, N., Bonneton, P., Dupuis, H., 2001a. Field observations of irregular wave transformation in the surf zone. In: Proc. Fourth Conf. Coast. Dyn. pp. 62–70.

Smit, P.B., Janssen, T.T., Herbers, T.H.C., Taira, T., Romanowicz, B.A., 2018. Infragravity wave radiation across the shelf break. JGR Oceans http://dx.doi.org/10.1029/2018JC013986.

Stockdon, H.F., Holman, R. a., Howd, P. a., Sallenger, A.H., 2006. Empirical parameterization of setup, swash, and runup. Coast. Eng. 53, 573–588.

Thompson, J., Elgar, S., Raubenheimer, B., Herbers, T.H.C., Guza, R.T., 2006. Tidal modulation of infragravity waves via nonlinear energy losses in the surfzone. Geophys. Res. Lett. 33, L05601. http://dx.doi.org/10.1029/2005GL025514.

Tissier, M., Bonneton, P., Michallet, H., Ruessink, B.G., 2015. Infragravity-wave modulation of short-wave celerity in the surf zone. J. Geophys. Res. Oceans 120, 6799–6814. http://dx.doi.org/10.1002/2015JC010708.

Tissier, M., Bonneton, P., Ruessink, B., 2017. Infragravity waves and bore merging. In: Proceedings of the Conference Coastal Dynamics 2017. ASCE, Helsingør, Denmark, pp. 451–460.

Tolman, H.L., 1991. A third-generation model for wind waves on slowly varying, unsteady and inhomogeneous depths and currents. J. Phys. Oceanogr. 21, 782–797.

Van Dongeren, A., Battjes, J., Janssen, T., van Noorloos, J., Steenhauer, K., Steenbergen, G., Reniers, A., 2007. Shoaling and shoreline dissipation of low-frequency waves. J. Geophys. Res. 112, C02011. http://dx.doi.org/10.1029/2006JC003701.

Vrećica, T., Soffer, R., Toledo, Y., 2019. Infragravity wave generation by wind gusts. Geophys. Res. Lett. 46 (16), 9728–9738.

Van Thiel de Vries, J., van Gent, R.A., Walstra, D.J., Reniers, A.J.H.M., 2008. Analysis of dune erosion processes in large-scale flume experiments. Coast. Eng. 55 (12), 1028–1040. http://dx.doi.org/10.1016/j.coastaleng.2008.04.004.